AGU PUBLICATIONS

Global Biogeochemical Cycles

RESEARCH ARTICLE
10.1002/2015GB005198

The scientific results and conclusions, as well as any views or opinions expressed herein, are those of the authors and do not necessarily reflect the views of NOAA or the Department of Commerce.

Key Points:
- Climatological aragonite saturation in surface and subsurface global oceans are presented
- Mechanisms controlling aragonite saturation state distributions are discussed
- Subannual and decadal changes of aragonite saturation state are presented

Supporting Information:
- Tables S1–S9

Correspondence to:
L.-Q. Jiang,
liqing.jiang@noaa.gov

Citation:
Jiang, L.-Q., R. A. Feely, B. R. Carter, D. J. Greeley, D. K. Gledhill, and K. M. Arzayus (2015), Climatological distribution of aragonite saturation state in the global oceans, *Global Biogeochem. Cycles*, *29*, doi:10.1002/2015GB005198.

Received 29 MAY 2015
Accepted 15 SEP 2015
Accepted article online 18 SEP 2015

Climatological distribution of aragonite saturation state in the global oceans

Li-Qing Jiang[1], Richard A. Feely[2], Brendan R. Carter[3], Dana J. Greeley[2], Dwight K. Gledhill[4], and Krisa M. Arzayus[5]

[1]Cooperative Institute for Climate and Satellites, Earth System Science Interdisciplinary Center, University of Maryland, College Park, Maryland, USA, [2]Pacific Marine Environmental Laboratory, National Oceanic and Atmospheric Administration, Seattle, Washington, USA, [3]Joint Institute for the Study of the Atmosphere and Ocean, University of Washington, Seattle, Washington, USA, [4]Ocean Acidification Program, National Oceanic and Atmospheric Administration, Silver Spring, Maryland, USA, [5]National Centers for Environmental Information, National Oceanic and Atmospheric Administration, Silver Spring, Maryland, USA

Abstract Aragonite saturation state (Ω_{arag}) in surface and subsurface waters of the global oceans was calculated from up-to-date (through the year of 2012) ocean station dissolved inorganic carbon (DIC) and total alkalinity (TA) data. Surface Ω_{arag} in the open ocean was always supersaturated ($\Omega > 1$), ranging between 1.1 and 4.2. It was above 2.0 (2.0–4.2) between 40°N and 40°S but decreased toward higher latitude to below 1.5 in polar areas. The influences of water temperature on the TA/DIC ratio, combined with the temperature effects on inorganic carbon equilibrium and apparent solubility product (K'_{sp}), explain the latitudinal differences in surface Ω_{arag}. Vertically, Ω_{arag} was highest in the surface mixed layer. Higher hydrostatic pressure, lower water temperature, and more CO_2 buildup from biological activity in the absence of air-sea gas exchange helped maintain lower Ω_{arag} in the deep ocean. Below the thermocline, aerobic decomposition of organic matter along the pathway of global thermohaline circulation played an important role in controlling Ω_{arag} distributions. Seasonally, surface Ω_{arag} above 30° latitudes was about 0.06 to 0.55 higher during warmer months than during colder months in the open-ocean waters of both hemispheres. Decadal changes of Ω_{arag} in the Atlantic and Pacific Oceans showed that Ω_{arag} in waters shallower than 100 m depth decreased by 0.10 ± 0.09 ($-0.40 \pm 0.37\%\,yr^{-1}$) on average from the decade spanning 1989–1998 to the decade spanning 1998–2010.

1. Introduction

The global oceans have performed a substantial climate service by taking up ~30% of the anthropogenic carbon dioxide (CO_2) emissions over the past 200 years [*Canadell et al.*, 2007]. Based on emission data from 2004 to 2013, CO_2 released from the burning of fossil fuels, cement production, and land use changes accounts for a total of $36\,GtCO_2\,yr^{-1}$ ($1\,GtCO_2 = 1 \times 10^{15}$ g of $CO_2 = 0.27 \times 10^{15}$ g of carbon). Of the CO_2 emitted during the last decade, about $16\,GtCO_2\,yr^{-1}$ (44%) stayed in the atmosphere, and $9\,GtCO_2\,yr^{-1}$ (26%) entered the global oceans [*Le Quéré et al.*, 2014]. The balance is assumed to be taken up by the terrestrial biosphere.

Ocean CO_2 uptake lowers ocean pH, carbonate ion (CO_3^{2-}) concentrations, and calcium carbonate ($CaCO_3$) saturation state in the global oceans. This process is commonly referred to as "ocean acidification (OA)" [*Broecker and Clark*, 2001; *Caldeira and Wickett*, 2003; *Feely et al.*, 2004a; *Orr et al.*, 2005]. OA impacts ecosystems by making it more difficult for calcifying organisms such as corals, mollusks, and some planktonic organisms to form shells and other hard parts and by making these structures more vulnerable to dissolution [*Doney et al.*, 2009; *Gattuso and Hansson*, 2011; *Bednaršek et al.*, 2012, 2014].

The saturation state of carbonate minerals is defined by

$$\Omega = \frac{[Ca^{2+}] \times [CO_3^{2-}]}{K'_{sp}} \quad (1)$$

where Ω is the saturation state ($\Omega > 1$ favors precipitation and $\Omega < 1$ favors dissolution), $[Ca^{2+}]$ and $[CO_3^{2-}]$ are the calcium and carbonate ion concentrations, and K'_{sp} is the apparent solubility product. The saturation states of aragonite and calcite (two of the most common calcium carbonate minerals in the ocean) dropped to ~84% of preindustrial values by the year 2000 and are expected to decrease to ~50% of preindustrial

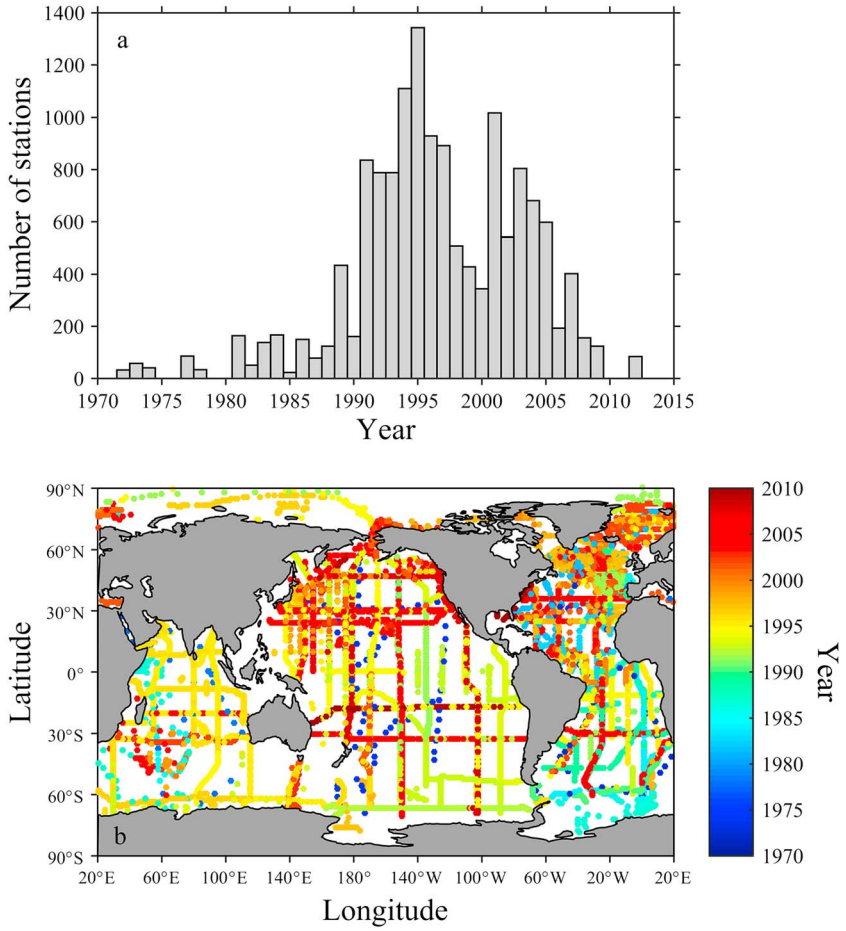

Figure 1. Information for the sampling stations that were used for this study: (a) number of sampling stations that were collected in a specific year and (b) spatial distributions of sampling stations. The color indicates the sampling year.

values by 2100 under the IS92a emission scenario of the Intergovernmental Panel on Climate Change report 1995 [*Wolf-Gladrow et al*., 1999; *Feely et al*., 2009b].

Surface aragonite and calcite saturation state distributions were studied by *Feely et al*. [2009a], using data from the Global Ocean Data Analysis Project (GLODAP) Version 1.1 (which includes data measured before 1999) [*Key et al*., 2004]. *Takahashi et al*. [2014] calculated surface aragonite and calcite saturation states (normalized to the year 2005) using partial pressure of carbon dioxide (pCO_2) data from the Lamont Doherty Earth Observatory database and total alkalinity (TA) estimated from sea surface salinity. However, the distributions of aragonite saturation states in subsurface waters have not been described in detail in the earlier studies.

We use additional data collected since the GLODAP version 1.1 release to reexamine the global aragonite saturation state. During this decade, ocean station data with multiple carbon parameters have nearly doubled (Figure 1a). Here we map and describe both surface and subsurface Ω_{arag} distributions in the global oceans, discuss the mechanisms controlling the Ω_{arag} distribution and seasonality, and estimate decadal Ω_{arag} changes in the major ocean basins.

2. Methods

Data for this study were obtained from the Global Ocean Data Analysis Project (GLODAP) [*Key et al*., 2004], the Carbon Dioxide in the Atlantic Ocean (CARINA) [*Key et al*., 2010], the Pacific Ocean Interior Carbon (PACIFICA) [*Suzuki et al*., 2013], and some recent cruise data sets [*Feely and Sabine*, 2011; *Wanninkhof et al*., 2014]. Duplicated stations—defined as stations with identical longitude, latitude, and sampling date—were

removed. Data with a salinity value of less than 25 (a total of about 30 stations) were excluded since most were measured in river plumes and do not reflect the open ocean. A total of 11,431 stations were selected for this study (Figure 1).

Ω_{arag} was calculated using a MATLAB version [*van Heuven et al*., 2009] of the CO2SYS program [*Lewis and Wallace*, 1998] based on equation (1). $[Ca^{2+}]$ in seawater was assumed to be conservative with salinity according to *Millero* [1995]:

$$\left[Ca^{2+}\right] = 293.86\, S \tag{2}$$

where the unit of $[Ca^{2+}]$ is $\mu mol\, kg^{-1}$, and S is salinity. $[CO_3{}^{2-}]$ was calculated from in situ temperature, pressure, salinity, dissolved inorganic carbon (DIC), total alkalinity (TA), silicate and phosphate with the dissociation constants for carbonic acid of *Lueker et al*. [2000], potassium bisulfate ($KHSO_4{}^-$) of *Dickson* [1990a], boric acid of *Dickson* [1990b], and the total borate concentration equations of *Lee et al*. [2010].

The apparent solubility product (K'_{sp}) of aragonite was calculated from temperature and salinity with the equation of *Mucci* [1983]. For surface waters at ambient pressure,

$$\begin{aligned} pK'_{sp} = {} & -[(-171.945 - 0.077993\, T + 2903.293/T + 71.595\, \log T) \\ & + (-0.068393 + 0.0017276\, T + 88.135/T)\, S^{0.5} - 0.10018\, S + 0.0059415\, S^{1.5}] \end{aligned} \tag{3}$$

where $pK'_{sp} = -\log K'_{sp}$, and T is temperature in kelvin (K). The pressure dependence of K'_{sp} is formulated in terms of the change in molal volume and compressibility as described in *Millero* [1995] using the corrected constants as presented in Appendix A.11 of *Zeebe and Wolf-Gladrow* [2001]:

$$\begin{aligned} pK'_{sp}{}^{P} = {} & pK'_{sp}{}^{0} - 0.434 \left\{ -\left[(-46 + 0.5304\, (T - 273.15)) / (RT) \times (P/10) \right] + 0.5 \right. \\ & \left. \times \left[(-0.011760 + 0.0003692\, (T - 273.15)) / (RT) \times (P/10)^2 \right] \right\} \end{aligned} \tag{4}$$

where the subscripts "0" and "*P*" on the solubility products denote conditions at the surface and at pressure P (dbar), respectively. The ideal gas constant R is 83.13 $cm^3\, bar\, (mol\, K)^{-1}$. More details of the saturation state calculation can be found in *Wanninkhof et al*. [2015].

Using the error propagation methods described in *Taylor* [1997], uncertainties of the calculated $[Ca^{2+}]$, $[CO_3{}^{2-}]$, and K'_{sp} were estimated to be 0.06%, 3.60%, and 0.00%, respectively. However, for K'_{sp}, the uncertainty is primarily from the use of an empirical equation to reflect the real-world K'_{sp}, rather than from propagating the uncertainties of T, S and P to the result of the equation of *Mucci* [1983]. According to *Mucci* [1983], the uncertainty of the former is much larger at about 5%. The two most cited measurements of the $[Ca^{2+}]/S$ ratio differ by ~0.1% [*Culkin and Cox*, 1966; *Riley and Tongudai*, 1967]. Despite other concerns related to local variability due to $CaCO_3$ dissolution/precipitation, and hydrothermal input, etc., the uncertainty of $[Ca^{2+}]$ can be assumed to be lower than 0.1% (A. Dickson, personal communication, 2015). Based on the above information, the uncertainty of aragonite saturation state was calculated as 6% according to equation (5):

$$\frac{\sigma_{\Omega_{arag}}}{\Omega_{arag}} = \sqrt{\left(\frac{\sigma_{[Ca^{2+}]}}{[Ca^{2+}]}\right)^2 + \left(\frac{\sigma_{[CO_3^{2-}]}}{[CO_3^{2-}]}\right)^2 + \left(\frac{\sigma_{K'_{sp}}}{K'_{sp}}\right)^2} \tag{5}$$

where σ represents the uncertainty of the calculated $[Ca^{2+}]$, $[CO_3{}^{2-}]$, and K'_{sp}. The uncertainty estimation was based on average temperature, salinity, DIC, and TA of 19.23°C, 34.87, 2020 $\mu mol\, kg^{-1}$, and 2306 $\mu mol\, kg^{-1}$, respectively, and the assumption that their uncertainties within the combined GLODAP, CARINA, and PACIFICA product were 0.01°C, 0.02, 4 $\mu mol\, kg^{-1}$, and 6 $\mu mol\, kg^{-1}$, respectively (R. M. Key, personal communication, 2015).

Ω_{arag} were corrected to a reference year of 2000 assuming that the seawater pCO_2 increase rate was 1.6 $\mu atm\, yr^{-1}$ in the surface mixed layer (SML) and that this rate linearly decreased to 0 $\mu atm\, yr^{-1}$ from the bottom of SML to 1000 m depth [*Sabine et al*., 2008]. The depth of SML was calculated as where the temperature change from the surface was 0.5°C [*Levitus*, 1982]. When Ω_{arag} distribution maps were plotted, only data with the closest sampling depths to the designated water depth were chosen. Stations where this distance exceeded 20 m (for depth layers between surface and 200 m) or 50 m (for depth levels deeper than 200 m) were discarded. The selected Ω_{arag} data at the designed water depth were then interpolated based on Data-Interpolating Variational Analysis (DIVA) using the default settings before they were plotted onto contour maps [*Troupin et al*., 2012]. Spatially interpolated values were also used to calculate area-averaged

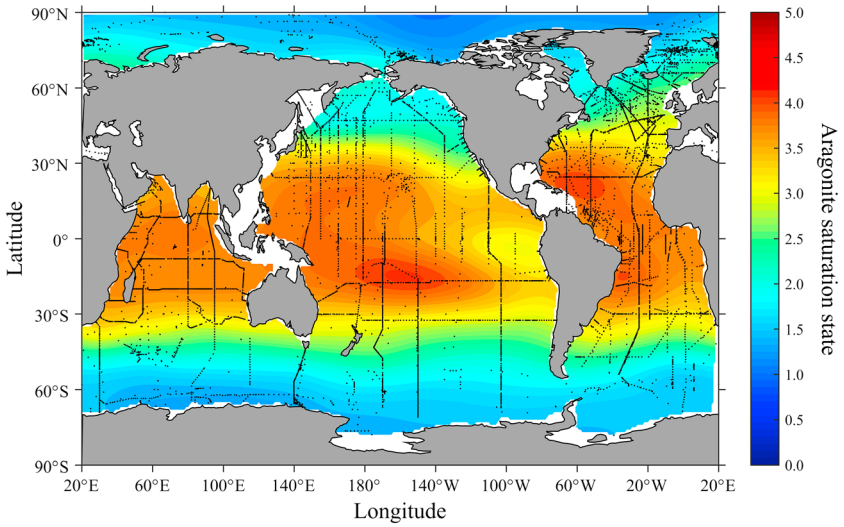

Figure 2. Climatological distributions of aragonite saturation state (Ω_{arag}) in surface waters of the global oceans. Colors show gridded values based on Data Interpolating Variational Analysis (DIVA). Black dots show the sampling stations.

Ω_{arag} at each latitudinal band of all depth levels (Tables S1–S9 in the supporting information) to correct for biases related to sampling coverage.

Seasonal measurement bias is one of the largest sources of uncertainty for the Ω_{arag} estimates. Seasonal variations of temperature, surface mixed layer (SML) depth, and spring blooms have a noticeable impact on Ω_{arag} in some regions of the global oceans. Due to the sampling strategies of the repeat hydrography cruises, very few stations had data from all seasons. When data were available from all seasons, they were often collected many years apart, making it hard to adjust for seasonal variations. Spatial measurement bias is also a concern, especially for the interpolated Ω_{arag} estimates.

3. Results

3.1. Spatial Distribution of Ω_{arag} at Different Depth Levels

Surface Ω_{arag} was always supersaturated ($\Omega > 1$), ranging between 1.1 and 4.1 (Figure 2 and Table S1). Area-weighted Ω_{arag} over the global ocean was 3.03. Surface Ω_{arag} showed similar spatial distribution to sea surface temperature (SST), with Ω_{arag} being highest where the surface ocean was warmest (Figure 2). Open-ocean Ω_{arag} was always above 2.0 (2.0–4.3) within 40° from the equator (40°N to 40°S) and decreased toward the poles (Figure 2). At latitudes >60° north and south, many areas had surface Ω_{arag} below 1.5. The range of Ω_{arag} of this study is similar to what was reported by *Takahashi et al.* [2014], i.e., Ω_{arag} was as high as 4.0 in the warm tropical and subtropical waters and as low as 1.2 in the cold subpolar and polar waters.

Ω_{arag} at 50 m depth was also supersaturated throughout the global ocean (Figure 3a and Table S2). One of the most conspicuous features at this depth was the unusually low Ω_{arag} values in the eastern equatorial Pacific region and along the west coast of North and South America (Figure 3a), where upwelling of CO_2-enriched waters is contributing to the decrease in Ω_{arag} along with anthropogenic CO_2 uptake [*Feely et al.*, 2008a, 2009a]. A similar process was occurring in the eastern boundary current systems in the eastern Atlantic Ocean [*Hill et al.*, 1998].

Ω_{arag} was supersaturated at 100 m depth except for 8.3% of gridded stations north of 50°N in the Pacific and 0.7% of gridded stations in the Arctic Ocean (Table S3). The extent of low Ω_{arag} areas in the equatorial oceans was significantly larger at 100 m depth than it was at 50 m depth (Figure 3b). Average Ω_{arag} between the latitudes of 10°N and 10°S in the Atlantic, Pacific, and Indian Oceans was 1.0, 0.7, and 1.0 lower, respectively, at 100 m depth than at 50 m depth (Table S3). Ω_{arag} in the eastern equatorial Pacific Ocean was lowest among the equatorial regions of the three basins at this depth (Figure 3b).

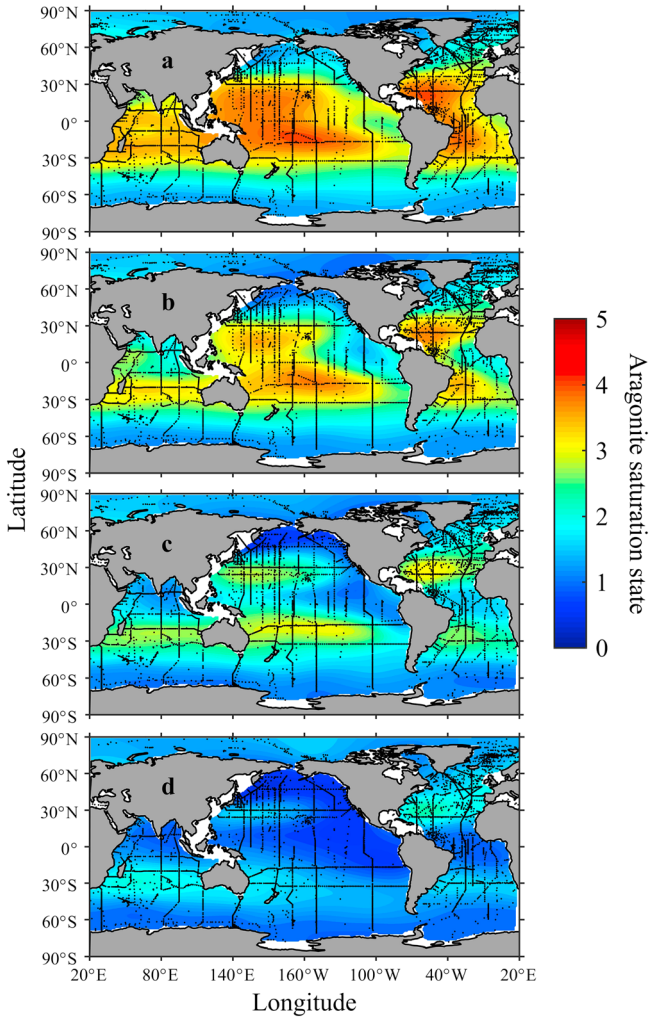

Figure 3. Spatial distributions of aragonite saturation state (Ω_{arag}) at depth levels of (a) 50 m, (b) 100 m, (c) 200 m, and (d) 500 m in the global oceans. Colors show gridded values based on Data Interpolating Variational Analysis (DIVA). Black dots show the sampling stations.

At 200 m depth, Ω_{arag} ranged between 0.5 and 3.2 (Figure 3c and Table S4). The low Ω_{arag} areas around the equator were larger at 200 m depth, and some gridded stations in the equatorial Pacific Ocean were as low as 1.0 (Table S4). The lowest regional Ω_{arag} was found north of 50°N in the Pacific Ocean, where 100% of the gridded stations were undersaturated. The latitudinal bands of 10°N–40°N and 10°S–40°S showed the greatest Ω_{arag} at this depth, with average Ω_{arag} within these latitudinal bands in the Atlantic and Pacific Oceans ranging between 2.0 and 2.7. The biggest differences in Ω_{arag} between the Atlantic and Pacific Oceans were found at the latitudinal band of 40°N–60°N (Figure 3c), where the average Ω_{arag} in the Atlantic Ocean (2.1) was more than double the Ω_{arag} in the Pacific Ocean (1.0). However, south of 10°N these two oceans had similar spatially averaged Ω_{arag} (Table S4).

At 500 m depth, Ω_{arag} ranged between 0.4 and 2.4 (Figure 3d and Table S5). Large areas of undersaturated Ω_{arag} were found between 40°N and 60°N in the northern Pacific Ocean, as well as in the equatorial Pacific Ocean (Figure 3d). The equatorial oxygen minimum zone was near its maximum extent between 500 m and 1000 m depth (Figure 4), suggesting that this depth was more strongly affected by CO_2 released through organic matter remineralization than deeper or shallower depths. Undersaturated waters were also found in the equatorial Atlantic and Indian Oceans. The average Ω_{arag} in the Atlantic Ocean between 20°N and 40°N (2.1) was ~90% higher than the average for the same latitudinal band in the Pacific Ocean (1.1). In comparison, Atlantic Ω_{arag} between 20°S and 40°S was only about 9% higher than those of the Pacific Ocean. The Indian Ocean showed the highest Ω_{arag} within the latitudinal band of 20°S to 40°S among the three ocean basins (Figure 3d).

At 1000 m depth, Ω_{arag} was below 1.8 over the entire global oceans (Figure 5a and Table S6). Ω_{arag} was undersaturated across the northern Pacific, most of the northern Indian Oceans, and some areas of the equatorial Atlantic and the Southern Ocean (Figure 5a). The greatest Ω_{arag} at this depth was found in the northern Atlantic Ocean from 30°N to 50°N, where Ω_{arag} ranged between 1.1 and 1.8 (Table S6). Arctic Ω_{arag} was mostly supersaturated (0.9–1.4) and ~25% higher than in the Southern Ocean.

At 2000 m depth, Ω_{arag} was undersaturated across all regions of the Pacific and the Indian Ocean (Figure 5b and Table S7). Atlantic Ω_{arag} was mostly >1 between 70°N and 10°S, although 100% of the gridded stations south of 30°S were undersaturated. One of the interesting features at this depth was the supersaturated Ω_{arag} region in the equatorial Atlantic Ocean (Figure 5b), which was found to be located above and below undersaturated waters (Figure 5a). Unusually low Ω_{arag} water from 500 m to 1000 m depth was found in Antarctic Intermediate Water (AAIW). This phenomenon will be discussed in greater detail in section 3.2 (Figure 4).

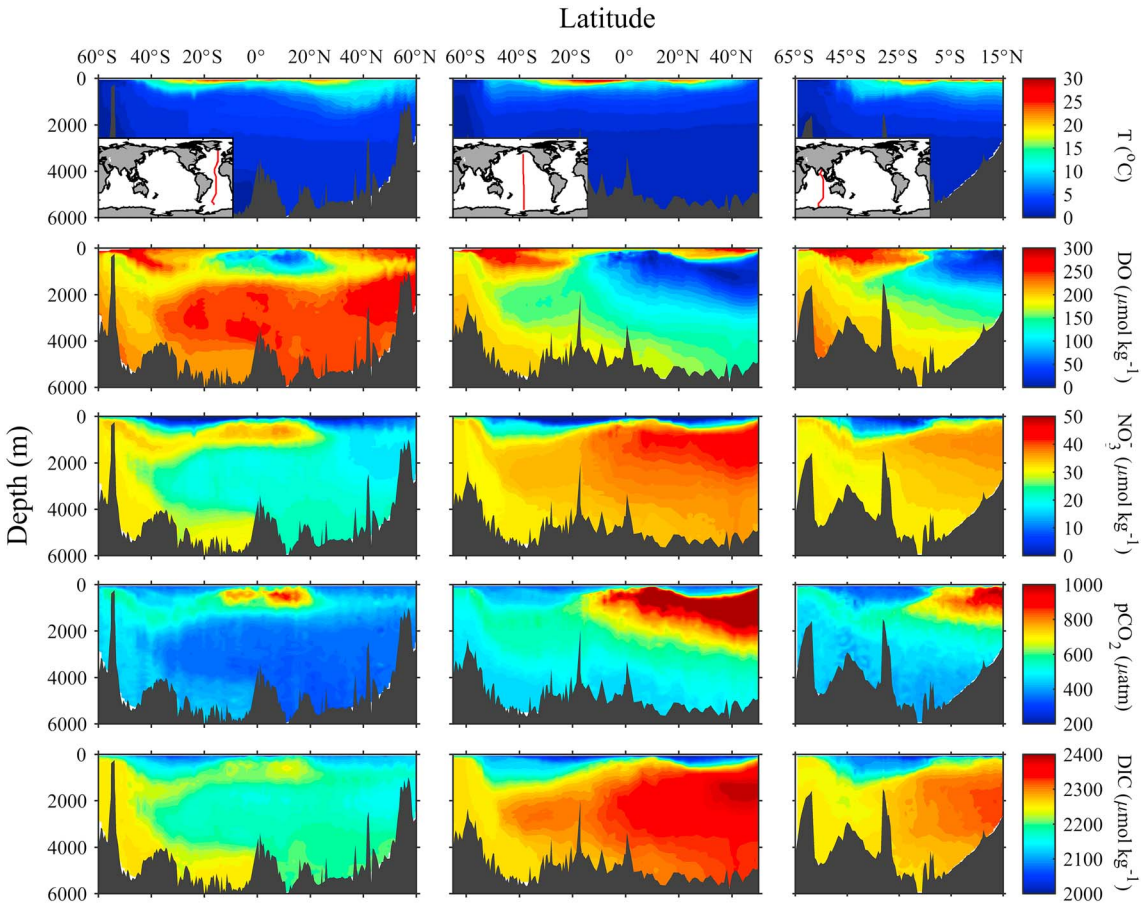

Figure 4. Vertical distributions of temperature (*T*), dissolved oxygen (DO), nitrate (NO_3^-), partial pressure of carbon dioxide (pCO_2), and dissolved inorganic carbon (DIC) in the Atlantic, Pacific, and Indian Oceans. Colors show gridded values from linear triangulation-based interpolation.

At 3000 m depth, Ω_{arag} all across the global oceans was undersaturated (Figure 5c and Table S8), with a range between 0.5 and 1.0. Atlantic Ω_{arag} was about 50–60% higher than Pacific Ω_{arag} within the latitudinal band of 10°N–70°N. This is because the dominant water mass in the deep North Atlantic is North Atlantic Deep Water (NADW), which is young compared to the Pacific Deep Water (PDW) and Circumpolar Deep Water (CDW) that dominate in the deep Pacific Ocean. Older PDW and CDW are richer in CO_2 from organic matter remineralization. Differences between Ω_{arag} in the Pacific and Atlantic Oceans diminished gradually toward the south, with no clear differences south of 50°S (Table S8) where all basins primarily contain CDW at this depth [*Talley*, 2013]. Indian Ocean Ω_{arag} was higher than Pacific Ocean Ω_{arag} but lower than Atlantic Ocean Ω_{arag} (Figure S8).

At 4000 m depth, Ω_{arag} had the lowest values and was undersaturated in all ocean basins (Figure 5d and Table S9). The differences between the Atlantic, Pacific, and Indian Oceans diminished significantly, as Ω_{arag} in the Atlantic Ocean dropped quicker with depth than that in the other two oceans. Ω_{arag} in the Atlantic, Pacific, and Indian Oceans were in the narrow ranges of 0.5–0.8, 0.5–0.7, and 0.5–0.7, respectively (Table S9).

3.2. Vertical Distributions of Ω_{arag}

Ω_{arag} decreased with increasing depth across most of the global oceans. The decrease was most pronounced in the shallow equatorial region due to the undersaturated waters brought up from the subsurface ocean by upwelling [*Feely et al*., 1999, 2006, 2009a]. In the Southern Ocean and northernmost (50°N–70°N) Atlantic Ocean, the decrease of Ω_{arag} with depth demonstrated a roughly linear relationship from surface to bottom. In contrast, Ω_{arag} in the northern Pacific (north of 50°N) decreased much faster from the surface to about 500 m depth than in the deep ocean (Figure 6).

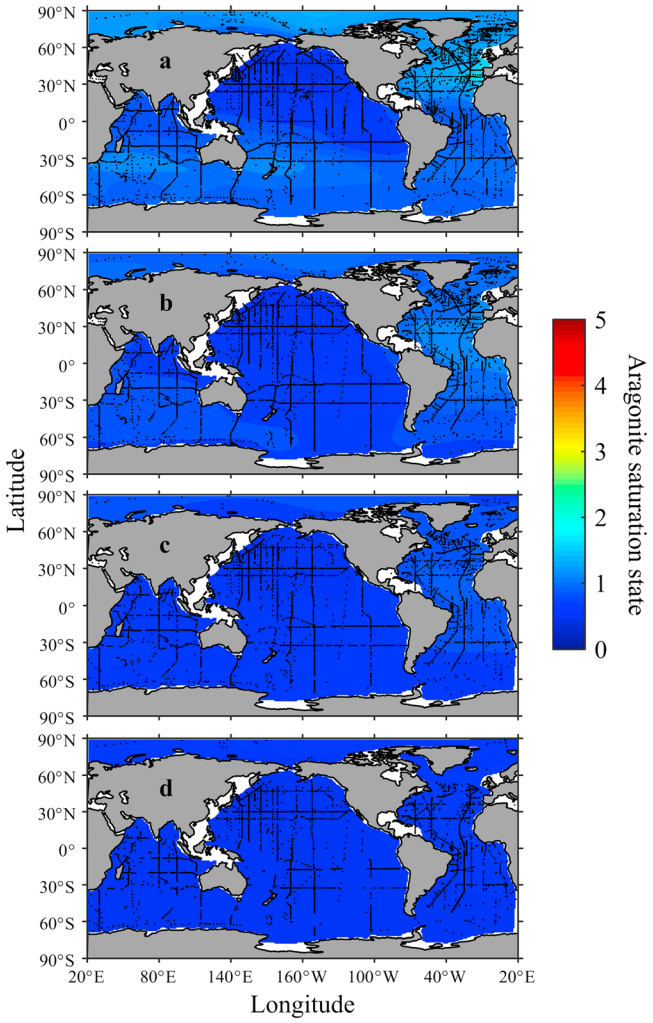

Figure 5. Spatial distributions of aragonite saturation state (Ω_{arag}) at depth levels of (a) 1000 m, (b) 2000 m, (c) 3000 m, and (a) 4000 m in the global oceans. Colors show gridded values based on Data Interpolating Variational Analysis (DIVA). Black dots show the sampling stations.

Vertical distributions of Ω_{arag} from three north-south transects of the Atlantic, Pacific, and Indian Oceans demonstrated clear differences between the Atlantic Ocean and the other two oceans (Figure 6). The aragonite saturation horizon, which is defined as the depth where Ω is equal to 1 (below the saturation horizon, Ω is less than 1; i.e., calcium carbonate is thermodynamically unstable and has a tendency to dissolve), was at a similar depth in the three ocean basins in the Southern Hemisphere. It ranged between 700 and 1500 m south of ~20°S and shoaled to about ~300–600 m near the equator. However, basin similarities disappeared north of 15°N. In the Atlantic, aragonite saturation horizon was around 2200–2500 m from 15°N to 60°N (Figure 6). In contrast, the deepest saturation horizon within the same latitudinal band in the North Pacific and North Indian Oceans was only about 500 m and 300 m, respectively (Figure 6). The saturation depths vary with longitude as well as latitude. Their west-east variations will be discussed later.

The distribution of aragonite saturation horizon depths can be understood in the context of global thermohaline circulation [*Broecker*, 1991] and organic matter remineralization [*Li et al*., 1969]. The depth of aragonite saturation horizon is inversely related to the age of the deep water in each basin, which is mapped by *Matsumoto and Key* [2004]. The deepest saturation horizon and youngest water are found in the North Atlantic. The shallowest saturation horizon and oldest deep waters are found in the North Pacific. This is because older water has had more time for CO_2 accumulation from organic matter remineralization.

Another important feature of the deep ocean is the undersaturated Ω_{arag} underneath the equatorial Atlantic Ocean (Figure 6). A tongue of low Ω_{arag} water between ~500 and 1000 m depth created an aragonite saturation horizon inversion, with supersaturated waters found both above and below the tongue (Figure 6). This water mass is Antarctic Intermediate Water (AAIW) that originates south of the Polar Frontal Zone [*Chung et al*., 2003]. We suspect that this phenomenon is related to a regional maximum in net organic matter remineralization (note the high nutrient and DIC concentrations and low dissolved oxygen in this tongue in Figure 4). While chlorofluorocarbon tracer ages calculated for the GLODAP data set [*Key et al*., 2004] suggest that these low O_2 waters are younger than the NADW below them, they are also closer to the surface where organic matter remineralization rates are higher.

Zonal Ω_{arag} sections were plotted in Figures 7–9. Both Atlantic transects showed weak west-east gradients (Figure 7). In the Indian Ocean, the aragonite saturation horizon shoaled slightly from west to east (Figure 8). This west to east trend was most prominent in the Pacific Ocean (Figure 9). At 30°N in the Pacific, the aragonite saturation horizon shoaled from ~750 m in the west to ~250 m in the east. At 20°S Pacific, it shoaled from ~1100 m off Australia to ~200 m near Peru (Figure 9).

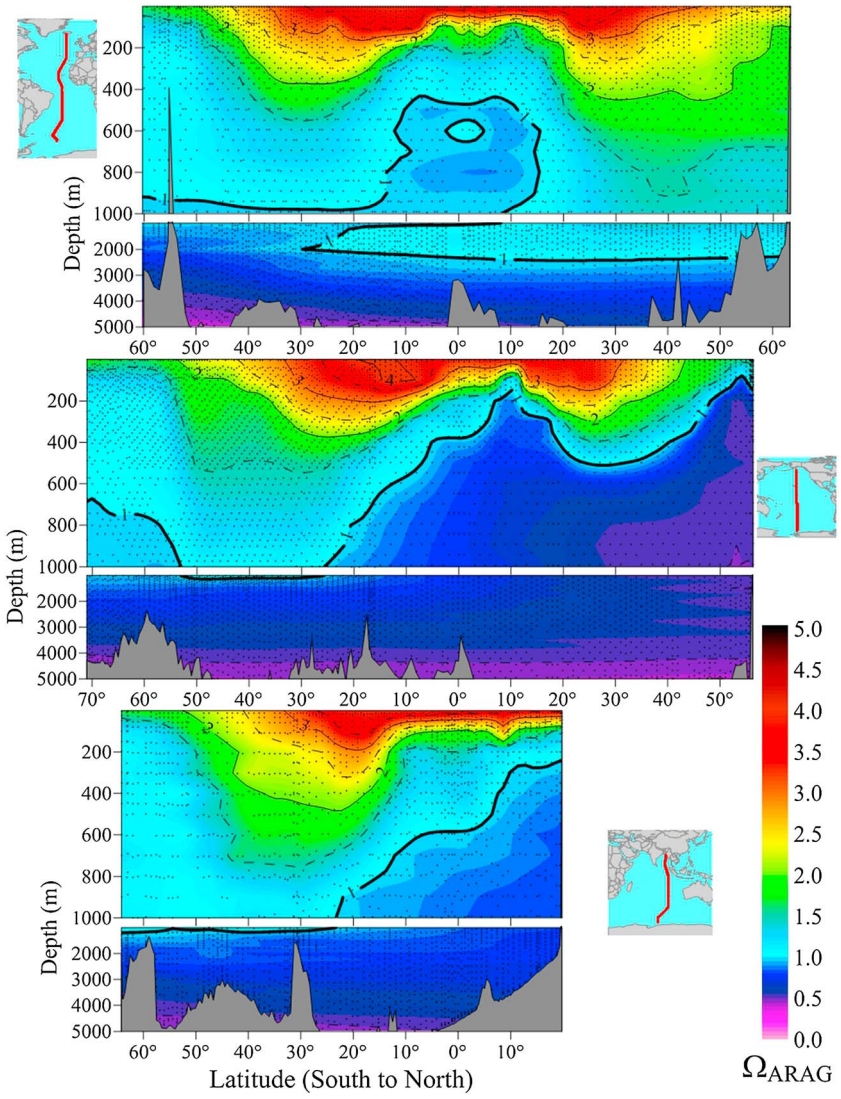

Figure 6. North to south vertical distributions of aragonite saturation state (Ω_{arag}) in the Atlantic, Pacific, and Indian Oceans. Colors show gridded values from linear triangulation-based interpolation. Solid and dashed lines show contour lines of aragonite saturation state. Black dots show where real data are available. The transect in the Atlantic Ocean is based on data from *Wanninkhof et al.* [2006] (EXPOCODE: 33RO20050111) and *Peltola et al.* [2005] (EXPOCODE: 33RO20030604). The transection in the Pacific Ocean is based on data from *Feely et al.* [2008b] (EXPOCODE: 33RR20050109 and 325020060213). The transect in the Indian Ocean is based on data from *Johnson et al.* [2002] (EXPOCODE: 316 N19941201).

The stark differences between the Pacific and Atlantic Oceans were due to their relative vertical locations of aragonite saturation horizon with respect to the base of the thermocline. In the Pacific Ocean, the aragonite saturation horizon was shallow and followed the 5°C isotherm (Figure 9), keeping it within the thermocline of the rapidly circulating subtropical gyre. Isopycnals in the Northern Pacific Subtropical Gyre are deeper in the west than in the east due to the geostrophic pressure gradient requirement [*McPhaden et al.*, 1998].

3.3. Seasonal Change in Surface Ω_{arag}

To examine the subannual cycles, we plotted surface Ω_{arag} using only data from the months of May to October (Figure 10a) and from November to March (Figure 10b). The results indicate that Ω_{arag} was consistently higher during the warmer months than during the colder months in the open-ocean waters of both hemispheres (Table 1). For example, Ω_{arag} between 30°N and 50°N in the North Atlantic Ocean was on average 0.21 higher during May to October than during November to March, and Ω_{arag} between 30°S and 50°S in the Southern Hemisphere was on average 0.23 higher during November to March than during May to

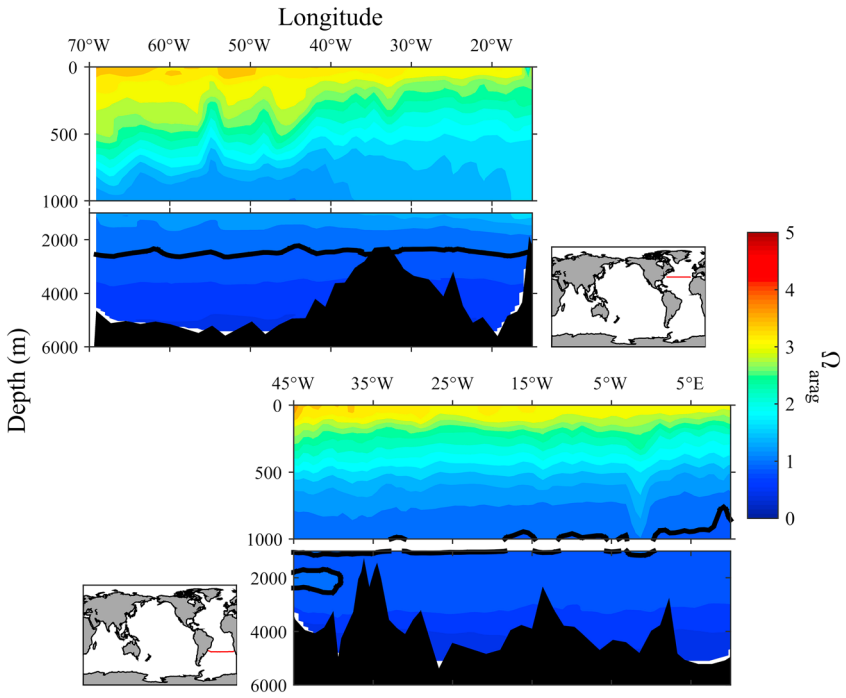

Figure 7. West to east vertical distributions of aragonite saturation state (Ω_{arag}) in the Atlantic Ocean. Colors show gridded values from linear triangulation-based interpolation. The solid black line shows where aragonite saturation state is equal to 1. The transect in the North Atlantic Ocean is based on data from *Schuster and Mcdonagh* [2007] (EXPOCODE: 74AB20050501). The transect in the South Atlantic Ocean is based on data from *Uchida et al.* [2005] (EXPOCODE: 49NZ20031106).

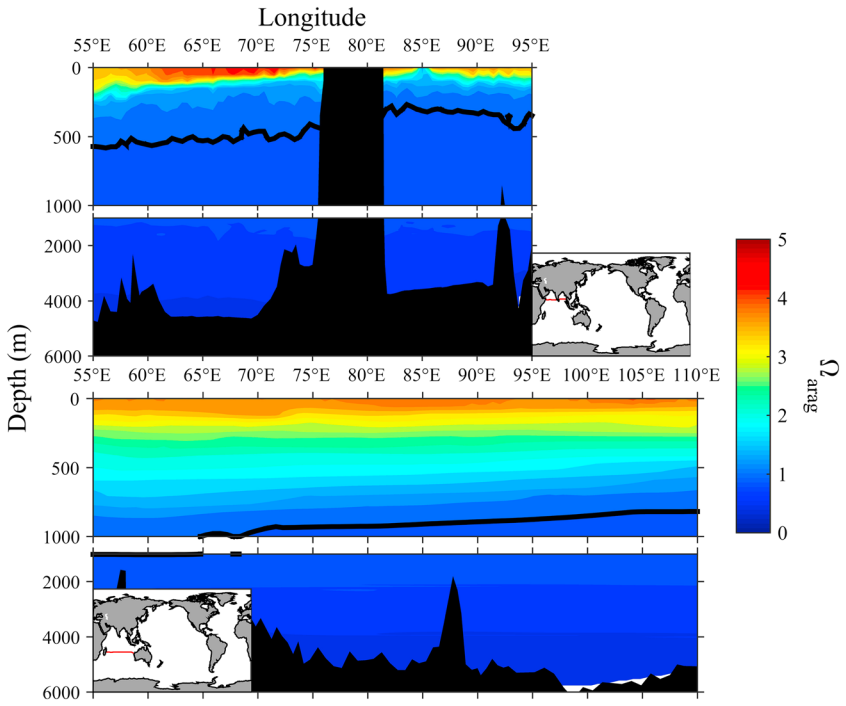

Figure 8. West to east vertical distributions of aragonite saturation state (Ω_{arag}) in the Indian Ocean. Colors show gridded values from linear triangulation-based interpolation. The solid black line shows where aragonite saturation state is equal to 1. The transect in the North Indian Ocean is based on data from *Johnson et al.* [2002] (EXPOCODE: 316 N19950829 and 316 N19950930). The transect in the South Indian Ocean is based on data from *Johnson et al.* [2002] (EXPOCODE: 316 N19950423).

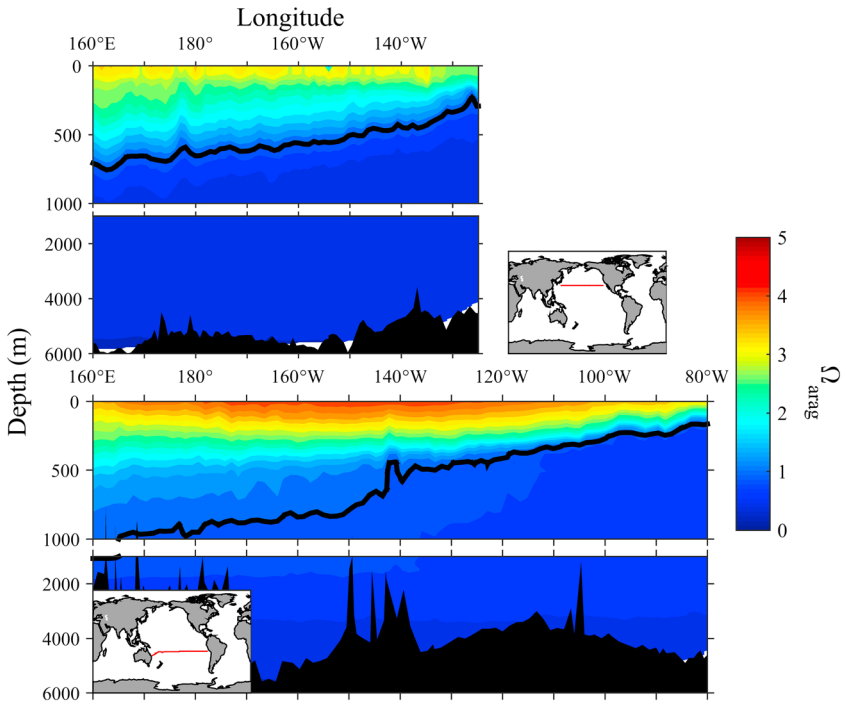

Figure 9. West to east vertical distributions of aragonite saturation state (Ω_{arag}) in the Pacific Ocean. Colors show gridded values from linear triangulation-based interpolation. The solid black line shows where aragonite saturation state is equal to 1. The transect in the North Pacific Ocean is based on data from *Feely et al.* [2004b] (EXPOCODE: 318 M200406). The transect in the South Pacific Ocean is based on data from *Uchida et al.* [2011] (EXPOCODE: 49NZ20090410, 49NZ20090521).

October (Table 1). The magnitude of seasonal variations of surface Ω_{arag} observed in this study (0.06–0.55) is similar to what was reported by *Takahashi et al.* [2014] in the global ocean and the upper open-ocean waters of the North Pacific Ocean (0.4–0.6) [*Kim et al.*, 2015].

In the coastal upwelling regions along the west coast of North and South America, the lowest aragonite saturation states were observed in summer rather than in winter (Figure 10a). This is due to the fact that the upwelling of CO_2-rich waters reaches their maximum strength in the late summer and early fall months [*Feely et al.*, 2008a; *Harris et al.*, 2013]. Similarly, low Ω_{arag} waters were observed in the summertime off the Canadian east coast near Newfoundland due to ice melt and freshwater input.

3.4. Decadal Changes of Ω_{arag} in the Pacific and Atlantic Oceans

Data in the Pacific and Atlantic Oceans allowed us to examine the decadal changes of Ω_{arag} in these regions. We compared spatially interpolated (1° × 1° grid) Ω_{arag} (without anthropogenic correction) from the sampling period January 1989 to June 1998 with the period June 1998 to December 2010. $\Delta\Omega_{arag}$ over the period was calculated as the difference of the gridded values in the period of 1998 to 2010 minus those in the period of 1989 to 1998. We observe large spatial variations (Figure 11), which are inevitable when using sparse gridded measurements to assess the combined influences of long-term trends (i.e., ocean acidification) as well as interannual cycles, seasonal variability, and daily cycles. In spite of the numerous unresolved modes of variability, we see bulk seawater chemistry changes that are consistent with the influence of ocean acidification.

The average surface (up to 100 m depth) Ω_{arag} in the Pacific Ocean changed by -0.12 ± 0.10 ($-0.48 \pm 0.42\%$) over the period (Table 2). This average value is close to the average Ω_{arag} change rate of $-0.34\%\,yr^{-1}$ observed at the same depth level in the Pacific Ocean by *Feely et al.* [2012]. Average surface (up to 100 m depth) Ω_{arag} in the Atlantic Ocean changed by -0.06 ± 0.03 ($-0.23 \pm 0.11\%\,yr^{-1}$) over the period (Table 3).

The combined basins changed by -0.10 ± 0.09 per decade or $-0.40 \pm 0.37\%\,yr^{-1}$ in depth levels from surface to 100 m. These averages were -0.09 ± 0.10 per decade or $-0.33 \pm 0.46\%\,yr^{-1}$ in depth range from surface to 200 m. We caution that these numbers are based on data from two adjacent 10 year periods, so differences in sample collection dates could range from 0 to 20 years.

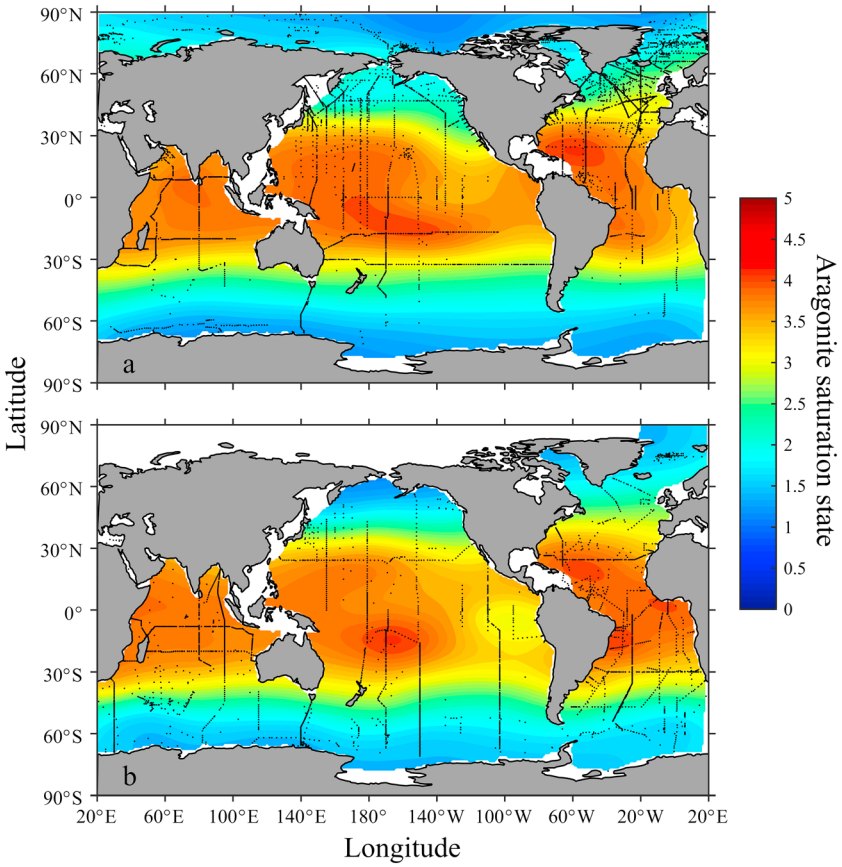

Figure 10. Spatial distributions of aragonite saturation state (Ω_{arag}) in surface waters of the global oceans based on data from (a) May to October and (b) November to March. Colors show gridded values based on Data Interpolating Variational Analysis (DIVA). Black dots show the sampling stations.

4. Discussion

4.1. Surface Ω_{arag} Versus SST

Temperature and Ω_{arag} have similar surface ocean distributions—high in the tropics and decreasing with latitude (Figure 2). Simple regression showed significant correlation in each ocean basin, with $R^2 = 0.94$ globally (Figure 12). Similar correlations between calcite saturation state and SST were reported by *Carter et al*. [2014] and attributed primarily to the influence of temperature on DIC in seawater at equilibrium with the atmosphere. In the following, we discuss the contributing factors to the correlation between surface Ω_{arag} and SST.

Calcium is found in a constant ratio to salinity [*Millero*, 1995]. We assume that its concentration has the same small relative standard deviation as salinity (~0.6% at the surface and less at depth [*Carter et al*., 2014]). Ω_{arag} is therefore primarily controlled by the carbonate ion concentration ($[CO_3^{2-}]$) and the apparent solubility product (K'_{sp}) (equation (1)).

When CO_2 enters the ocean, a portion of the dissolved carbon dioxide reacts with water to form carbonic acid (H_2CO_3). Some of the carbonic acid then dissociates, generating hydrogen ions (H^+) and bicarbonate ions (HCO_3^-). Most of that H^+ combines with carbonate ion (CO_3^{2-}) to form more bicarbonate ions (HCO_3^-). The processes can be simplified into one equation:

$$CO_2 + H_2O + CO_3^{2-} \rightleftharpoons 2HCO_3^- \quad (6)$$

when water temperature increases, the equilibrium (equation (6)) shifts to the left, increasing the carbonate ion concentration ($[CO_3^{2-}]$) and elevating Ω_{arag} [*Dickson and Millero*, 1987].

Apparent solubility product (K'_{sp}) is mainly dependent on temperature in the surface ocean. The K'_{sp} for aragonite decreases by about 11.5% from 5°C to 35°C or ~0.4%/°C [*Mucci*, 1983]. Therefore, like the temperature

Table 1. Spatially Averaged Surface Aragonite Saturation State (Ω_{arag}) Within Latitudinal Bands of Major World Ocean Basins at Different Times of the Year[a]

Season	Latitude	Atlantic Ocean	Pacific Ocean	Indian Ocean
Ω_{arag} during Nov to Mar	70°N to 90°N	1.61 (1.38 to 1.92)	n/a	n/a
	50°N to 70°N	2.08 (1.55 to 2.60)	1.47 (1.17 to 1.80)	n/a
	30°N to 50°N	3.17 (2.49 to 3.79)	2.53 (1.57 to 3.42)	n/a
	10°N to 30°N	3.87 (3.34 to 4.05)	3.59 (2.96 to 3.87)	3.72 (3.47 to 3.88)
	10°S to 10°N	3.95 (3.80 to 4.04)	3.73 (3.23 to 4.06)	3.86 (3.73 to 3.91)
	30°S to 10°S	3.73 (3.24 to 4.08)	3.75 (3.14 to 4.11)	3.74 (3.33 to 3.90)
	50°S to 30°S	2.81 (1.89 to 3.60)	2.83 (2.04 to 3.58)	3.06 (2.01 to 3.74)
	Southernmost to 50°S	1.79 (1.55 to 2.42)	1.78 (1.42 to 2.40)	1.60 (1.41 to 2.12)
Ω_{arag} during May to Oct	70°N to 90°N	1.85 (1.25 to 2.40)	n/a	n/a
	50°N to 70°N	2.37 (1.80 to 2.92)	2.02 (1.86 to 2.18)	n/a
	30°N to 50°N	3.27 (2.36 to 3.95)	2.73 (1.92 to 3.62)	n/a
	10°N to 30°N	3.91 (3.41 to 4.12)	3.68 (2.65 to 3.95)	3.74 (3.58 to 3.91)
	10°S to 10°N	3.76 (3.45 to 3.94)	3.83 (3.51 to 4.04)	3.85 (3.65 to 3.94)
	30°S to 10°S	3.57 (2.97 to 3.91)	3.76 (3.07 to 4.07)	3.66 (3.10 to 3.88)
	50°S to 30°S	2.56 (1.85 to 3.33)	2.62 (1.96 to 3.27)	2.82 (1.90 to 3.49)
	Southernmost to 50°S	1.61 (1.35 to 1.99)	1.66 (1.22 to 2.11)	1.51 (1.23 to 1.99)
Delta Ω_{arag} (Ω_{arag} during May to Oct − Ω_{arag} during Nov to Mar)	70°N to 90°N	0.24 (−0.19 to 0.53)	n/a	n/a
	50°N to 70°N	0.29 (−0.12 to 0.58)	0.55 (0.25 to 0.93)	n/a
	30°N to 50°N	0.10 (−0.13 to 0.33)	0.20 (−0.34 to 0.55)	n/a
	10°N to 30°N	0.04 (−0.19 to 0.16)	0.09 (−0.33 to 0.34)	0.02 (−0.25 to 0.21)
	10°S to 10°N	−0.18 (−0.45 to 0.03)	0.18 (−0.04 to 0.63)	−0.01 (−0.23 to 0.11)
	30°S to 10°S	−0.17 (−0.45 to −0.04)	0.05 (−0.46 to 0.57)	−0.09 (−0.33 to 0.08)
	50°S to 30°S	−0.25 (−0.66 to −0.04)	−0.23 (−0.57 to −0.01)	−0.18 (−0.38 to 0.25)
	Southernmost to 50°S	−0.18 (−0.43 to −0.04)	−0.13 (−0.36 to −0.01)	−0.06 (−0.24 to 0.25)

[a]Format: area-averaged mean value (minimum value − maximum value). The mean, minimum, and maximum values are based on Data Interpolating Variational Analysis (DIVA).

effect on $[CO_3^{2-}]$, the temperature dependence of K'_{sp} also contributes positively to the linear relationship between surface Ω_{arag} and SST.

To examine whether the temperature effects on $[CO_3^{2-}]$ and K'_{sp} could explain the linear correlations between Ω_{arag} and SST, temperature-normalized Ω_{arag} was calculated from in situ temperature, salinity, DIC, and TA, with an output temperature of 19°C. These two temperature effects explained about 23% of the latitudinal Ω_{arag} gradient. After temperature normalization, Ω_{arag} still showed a positive slope with increasing temperature (Figure 13), suggesting that additional effects must be important.

Thus far, the discussion has not considered the influence of temperature on TA/DIC ratio through CO_2 exchange, and the subsequent influence on $[CO_3^{2-}]$. The global surface ocean is a dynamic system with various CO_2 input/output processes, including air-sea gas exchange, photosynthesis/respiration, and exchange with the deep ocean. However, what determines the CO_2 contents ultimately staying in a body of water is mainly the capacity of the water to react with CO_2 chemically (equation (6)). For a body of water to maintain a certain pCO_2 level, lower water temperature requires higher DIC than higher water temperature. The higher DIC relative to a constant TA (lower TA/DIC ratio) in colder water translates to lower $[CO_3^{2-}]$ and lower Ω_{arag}. In the following, we try to quantify whether this third temperature effect could help explain the rest of the latitudinal surface Ω_{arag} gradient.

If we remove all three temperature effects on the in situ Ω_{arag}, any residual correlation between Ω_{arag} and SST should be coincidental. We remove all three effects in two steps: We calculated pCO_2 from in situ temperature, salinity, TA, and DIC. We then reset the global surface water temperature to a constant 19°C everywhere and allowed the water to exchange CO_2 through processes that do not change TA until the pCO_2 was back to the same level as before the temperature was reset to 19°C. Under these scenarios, the calculated Ω_{arag} based on an input temperature of 19°C, the original salinity, TA, and the calculated pCO_2 from the first step was the normalized surface Ω_{arag} with all three temperature effects removed. The results show that the slopes between the temperature-normalized Ω_{arag} and SST were reduced to values that were statistically indistinguishable from zero (Figure 13).

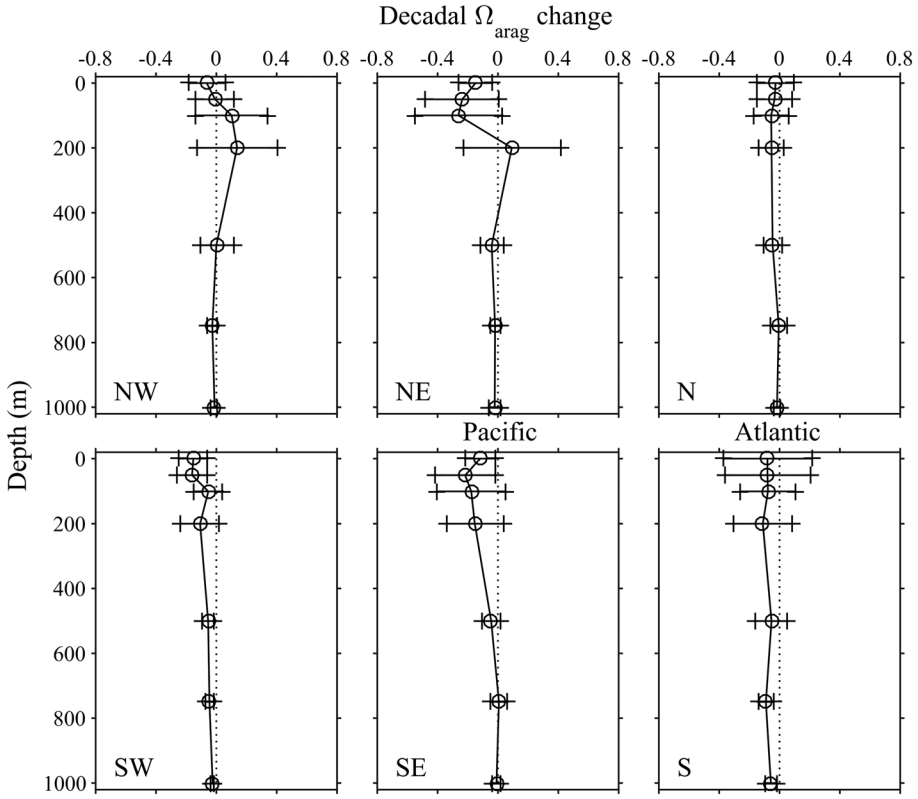

Figure 11. The mean differences of spatially interpolated (1° × 1° grid) aragonite saturation state (Ω_{arag}) between measurements from 1989 to June 1998 and measurements from July 1998 to 2010 in the northwestern (NW), northeastern (NE), southwestern (SW), and southeastern (SE) sections of the Pacific Ocean, as well as northern (N) and southern (S) sections of the Atlantic Ocean. The error bars show the standard deviations of the delta aragonite saturation states.

4.2. Ω_{arag} in the SML Versus the Deep Ocean

Within the global oceans the permanent thermocline separates the surface mixed layer (SML) from the deep ocean; Ω_{arag} in the SML was mostly higher than in the deep ocean, although the vertical gradients generally decreased toward the poles (Figure 6). The SML is different from the deep ocean because of (1) its higher water temperature and lower hydrostatic pressure, (2) its exposure to sunlight allowing photosynthesis, and (3) its exchange of gases with the atmosphere.

Two differences between the SML and the deep ocean are water temperature and hydrostatic pressure. Water temperature can vary from over 30°C in the surface to below 0°C at the bottom of the oceans. Imagine if we could move all of the global surface waters to 4000 m depth and reset the water temperature to 1.5°C; the $\Delta\Omega_{arag}$ due to these two factors (temperature and hydrostatic pressure changes) alone would be between 1.0 (polar areas) and 2.4 units (equatorial areas). That is equivalent to 73–82% of the actual Ω_{arag} change from surface to 4000 m depth. Of these two factors, hydrostatic pressure dominates. In the equatorial regions, the effect of hydrostatic pressure change (from surface to 4000 m depth) on $\Delta\Omega_{arag}$ is about 4 times larger than the effect of temperature change (from SST to 1.5°C). Moving toward the poles, the relative importance of hydrostatic pressure increases quickly to the extent that the small effect of temperature is essentially unimportant.

The availability of sunlight in the euphotic zone (0–200 m) allows photosynthesis to occur. Photosynthesis takes up CO_2 from the surface and forms organic matter. Some of the produced organic matter sinks to the deeper layers in the form of particles or as dissolved carbon entrained in the sinking water. The organic matter is then remineralized at depth, releasing CO_2. This "biological pump" plays an important role in decreasing the DIC concentration in the SML and increasing the DIC concentration in the deep ocean, hence maintaining the Ω_{arag} gradient between the SML and the deep ocean.

Table 2. Temporal Changes of Aragonite Saturation State in the Northwestern (NW), Northeastern (NE), Southwestern (SW), and Southeastern (SE) Sections of the Pacific Ocean[a]

Region	Depth	1989 to Jun 1998	Jun 1998 to 2010	Ω_{arag} Change in 10 Years	Annual Ω_{arag} Change (%)	Standard Deviation of Ω_{arag}	CO_3^{2-} Change in 10 Years (μmol kg^{-1})	DIC Change in 10 Years (μmol kg^{-1})
NW Pacific	0	3.31	3.25	−0.06	−0.19	0.12	−3.3	21.8
	50	3.08	3.07	−0.01	−0.03	0.13	−0.6	9.5
	100	2.62	2.72	0.10	0.38	0.24	5.8	−2.6
	200	1.83	1.97	0.14	0.72	0.26	8.6	−9.8
	500	1.03	1.03	0.00	0.01	0.11	−0.1	0.8
	750	0.71	0.69	−0.03	−0.37	0.04	−1.9	5.9
	1000	0.64	0.63	−0.01	−0.18	0.02	−1.0	2.9
NE Pacific	0	3.15	3.00	−0.15	−0.47	0.11	−8.8	15.0
	50	2.87	2.64	−0.23	−0.84	0.24	−14.9	30.6
	100	2.19	1.94	−0.26	−1.24	0.29	−17.2	34.8
	200	1.38	1.47	0.09	0.64	0.32	5.5	−3.5
	500	0.79	0.74	−0.04	−0.53	0.07	−3.0	5.6
	750	0.64	0.62	−0.02	−0.30	0.03	−1.6	1.1
	1000	0.64	0.62	−0.02	−0.34	0.04	−1.7	4.8
SW Pacific	0	2.88	2.73	−0.15	−0.54	0.09	−9.2	20.9
	50	2.81	2.65	−0.16	−0.58	0.09	−9.8	19.5
	100	2.52	2.47	−0.05	−0.21	0.10	−3.4	6.6
	200	2.10	1.99	−0.11	−0.52	0.13	−7.5	15.1
	500	1.37	1.32	−0.05	−0.40	0.04	−4.0	9.0
	750	1.13	1.09	−0.04	−0.40	0.03	−3.2	5.0
	1000	1.01	0.99	−0.02	−0.24	0.01	−2.0	−0.1
SE Pacific	0	2.73	2.62	−0.12	−0.43	0.10	−7.3	8.7
	50	2.68	2.46	−0.22	−0.84	0.20	−13.4	14.1
	100	2.39	2.21	−0.17	−0.76	0.22	−11.4	12.8
	200	1.92	1.77	−0.15	−0.82	0.19	−10.4	15.9
	500	1.17	1.13	−0.04	−0.38	0.06	−3.2	7.9
	750	1.03	1.03	0.01	0.06	0.06	0.3	−2.5
	1000	0.92	0.91	−0.01	−0.10	0.03	−0.7	0.4

[a]The four sections were divided from the equator and 160°W. The mean values are based on Data Interpolating Variational Analysis (DIVA).

"Solubility pump" (physical and chemical transport of inorganic carbon to the deep ocean) plays another important role in contributing to the Ω_{arag} gradient between the surface and the deep ocean. The thermohaline circulation is driven by the formation of deep water at high latitudes where seawater is colder (promotes higher CO_2 absorbing capability) and denser (promotes sinking) [*Broecker*, 1991]. These two processes act together to pump CO_2 from the surface to the deep ocean.

Table 3. Temporal Changes of Aragonite Saturation State (Ω_{arag}), Carbonate ion (CO_3^{2-}), and Dissolved Inorganic Carbon (DIC) in the Northern (N) and Southern (S) Sections of the Atlantic Ocean[a]

Region	Depth	1989 to Jun 1998	Jun 1998 to 2010	Ω_{arag} Change in 10 Years	Annual Ω_{arag} Change (%)	Standard Deviation of Ω_{arag} Change	CO_3^{2-} Change in 10 Years (μmol kg^{-1})	DIC Change in 10 Years (μmol kg^{-1})
Northern Atlantic	0	2.99	2.97	−0.03	−0.09	0.12	−1.6	−3.4
	50	2.77	2.74	−0.03	−0.12	0.11	−2.0	1.5
	100	2.44	2.39	−0.05	−0.22	0.12	−3.7	5.3
	200	2.09	2.04	−0.05	−0.26	0.08	−3.6	5.4
	500	1.63	1.58	−0.05	−0.28	0.06	−3.3	5.2
	750	1.34	1.33	0.00	−0.04	0.05	−0.7	1.8
	1000	1.25	1.24	−0.02	−0.13	0.03	−1.2	1.5
Southern Atlantic	0	2.70	2.62	−0.08	−0.30	0.29	−4.3	−1.0
	50	2.59	2.51	−0.08	−0.31	0.28	−4.7	−4.7
	100	2.20	2.13	−0.08	−0.35	0.18	−5.1	−2.7
	200	1.81	1.70	−0.11	−0.62	0.19	−7.7	2.4
	500	1.26	1.21	−0.05	−0.42	0.11	−3.8	4.2
	750	1.12	1.03	−0.09	−0.83	0.05	−6.9	15.3
	1000	1.02	0.96	−0.06	−0.57	0.04	−4.6	7.3

[a]The two regions are divided from the equator. The mean values are based on Data Interpolating Variational Analysis (DIVA).

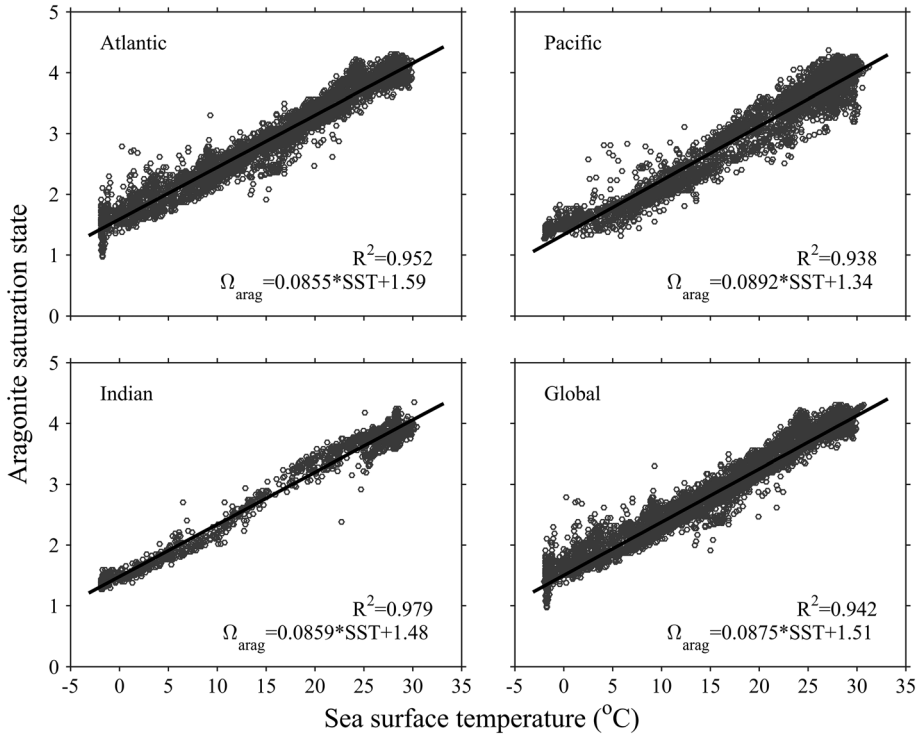

Figure 12. Regression of surface water aragonite saturation state (Ω_{arag}) against sea surface temperature (SST). The black circles represent individual data points from all sampling stations. The solid black lines show the linear relationship between Ω_{arag} and SST. Standard deviations of the linear regression slopes in the Atlantic, Pacific, Indian, and the global oceans are 0.0003, 0.0004, 0.0003, and 0.0001, respectively.

Below the permanent thermocline, air-sea gas exchange is virtually shut off and photosynthesis rarely takes place due to the lack of light, leaving aerobic respiration as the main process contributing to the low Ω_{arag} in the deep water [*Carter et al*., 2014]. Remineralization decreases Ω_{arag} by releasing CO_2 to the water, shifting the inorganic carbon equilibrium (equation (6)) to the right and decreasing [CO_3^{2-}]. More details will be discussed in the next section.

4.3. Ω_{arag} in the Atlantic Versus the Pacific and Indian Oceans

One of the most striking features of Ω_{arag} in the deep ocean is the much deeper saturation depths in the North Atlantic compared with those in the North Pacific and North Indian Oceans (Figures 6–9). The significant difference in aragonite saturation horizons between the Atlantic Ocean and the Pacific and Indian Oceans can be explained by the global thermohaline circulation (or Ocean Conveyor Belt) theory [*Broecker*, 1991]. The young surface water, containing relatively high concentrations of organic matter and dissolved oxygen (DO), sinks at the high-latitude regions of the North Atlantic, forming the NADW. It then flows southward all the way to Antarctica, through the Indian Ocean to the Pacific where, eventually, it rises to shallow depths in the North Pacific. The whole process takes about 1000 years to complete [*Broecker*, 1991]. During the long journey, the organic matter sinking from the euphotic surface mixed layer is slowly remineralized, consuming oxygen, producing CO_2, and lowering Ω_{arag}. The increase of NO_3^-, pCO_2, and DIC and the decrease of DO from north to south in the deep waters of the Atlantic Ocean and from south to north in the deep waters of the Pacific and Indian Oceans can be clearly seen from Figure 4.

5. Summary

The climatological distribution of Ω_{arag} in the global oceans was determined by compiling the available ocean station data with both DIC and TA measurements. The influence of water temperature on the TA/DIC ratio, combined with the temperature effects on inorganic carbon equilibrium and apparent solubility product (K'_{sp}), explain a large portion of the latitudinal differences in surface Ω_{arag}. Below the thermocline,

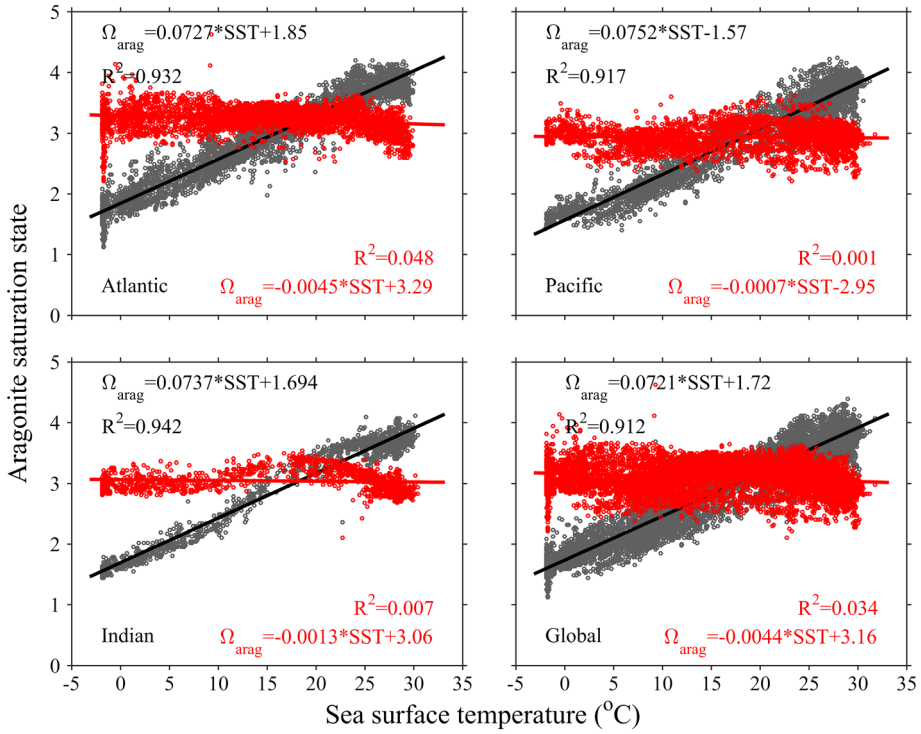

Figure 13. Regression of temperature (19°C)-normalized surface aragonite saturation state (Ω_{arag}) against sea surface temperature (SST). The black dots are from temperature normalization that only removes the effects of temperature on inorganic carbon equilibrium and apparent stoichiometric solubility product (K_{sp}). The red dots are from temperature normalization that removes all aspects of the temperature effects, including the CO_2 exchanges that are caused by latitudinal SST gradient-induced CO_2 solubility differences. The solid black and red lines show their corresponding linear relationships.

increasing pressure, decreasing temperature, and remineralization of organic matter along the pathway of global thermohaline circulation played important roles in controlling the Ω_{arag} distributions. On a seasonal basis, surface Ω_{arag} above 30° latitudes were about 0.06 to 0.55 higher during warmer months than during colder months in the open-ocean waters of both hemispheres. Decadal changes of Ω_{arag} indicated that waters shallower than 100 m depth decreased by 0.10 ± 0.09 ($-0.40 \pm 0.37\%\ yr^{-1}$) on average over the period of 1989–1998 to 1998–2010.

Acknowledgments

Data of this study came from the Carbon Dioxide in the Atlantic Ocean (CARINA), the Pacific Ocean Interior Carbon (PACIFICA), the Global Ocean Data Analysis Project (GLODAP), and some recent cruise data sets [*Feely and Sabine*, 2011; *Wanninkhof et al.*, 2014]. All of the data used are available at the Carbon Dioxide Information Analyses Center. We acknowledge funding support from the National Oceanic and Atmospheric Administration (NOAA)'s Ocean Acidification Program, the Climate Observations Division of NOAA's Climate Program Office, NOAA's Pacific Marine Environmental Laboratory (contribution 4278), and the Global Ocean Acidification Observing Network (contribution 0001). We thank Rik Wanninkhof of NOAA's Atlantic Oceanographic and Meteorological Laboratory and Robert M. Key of Princeton University for their tremendous contribution to the analysis of data and comments on earlier versions of the manuscript. We are grateful to Andrew Dickson of Scripps Institution of Oceanography for help with the error analysis. We thank Tim Boyer of the NOAA's National Centers for Environmental Information and Siv Lauvset of University of Bergen for exploration of gridding options. We thank Ernie Lewis of Brookhaven National Laboratory for guidance on the use of CO2SYS to calculate carbonate parameters.

References

Bednaršek, N., et al. (2012), Extensive dissolution of live pteropods in the Southern Ocean, *Nat. Geosci.*, *5*, 881–885.

Bednaršek, N., R. A. Feely, J. C. P. Reum, B. Peterson, J. Menkel, S. R. Alin, and B. Hales (2014), *Limacina helicina* shell dissolution as an indicator of declining habitat suitability due to ocean acidification in the California Current Ecosystem, *Proc. R. Soc. B*, *281* 20140123, doi:10.1098/rspb.2014.0123.

Broecker, W., and E. Clark (2001), A dramatic Atlantic dissolution event at the onset of the last glaciation, *Geochem. Geophys. Geosyst.*, *2*(11), 1065, doi:10.1029/2001GC000185.

Broecker, W. S. (1991), The great ocean conveyor, *Oceanography*, *4*, 79–89.

Caldeira, K., and M. E. Wickett (2003), Oceanography: Anthropogenic carbon and ocean pH, *Nature*, *425*, 365.

Canadell, J. G., C. Le Quere, M. R. Raupach, C. B. Field, E. T. Buitenhuis, P. Ciais, T. J. Conway, N. P. Gillett, R. A. Houghton, and G. Marland (2007), Contributions to accelerating atmospheric CO_2 growth from economic activity, carbon intensity, and efficiency of natural sinks, *Proc. Natl. Acad. Sci. U.S.A.*, *104*, 18,866–18,870.

Carter, B. R., J. R. Toggweiler, R. M. Key, and J. L. Sarmiento (2014), Processes determining the marine alkalinity and calcium carbonate saturation state distributions, *Biogeosciences*, *11*, 1–14.

Chung, S.-N., K. Lee, R. A. Feely, C. L. Sabine, F. J. Millero, R. Wanninkhof, J. L. Bullister, R. M. Key, and T.-H. Peng (2003), Calcium carbonate budget in the Atlantic Ocean based on water column inorganic carbon chemistry, *Global Biogeochem. Cycles*, *17*(4), 1093, doi:10.1029/2002GB002001.

Culkin, F., and R. A. Cox (1966), Sodium, potassium, magnesium, calcium and strontium in seawater, *Deep Sea Res.*, *13*, 789–804.

Dickson, A. G. (1990a), Standard potential of the reaction: AgCl(s) + 1/2 H_2(g) = Ag(s) + HCl(aq), and the standard acidity constant of the ion HSO_4^- in synthetic seawater from 273.15 to 318.15K, *J. Chem. Thermodyn.*, *22*, 113–127.

Dickson, A. G. (1990b), Thermodynamics of the dissociation of boric acid in synthetic sea water from 273.15 to 318.15 K, *Deep Sea Res.*, *37*, 755–766.

Dickson, A. G., and F. J. Millero (1987), A comparison of the equilibrium constants for the dissociation of carbonic acid in seawater media, *Deep Sea Res.*, *34*, 1733–1743.
Doney, S. C., V. J. Fabry, R. A. Feely, and J. A. Kleypas (2009), Ocean acidification: The other CO_2 problem, *Annu. Rev. Mar. Sci.*, *1*, 169–192.
Feely, R. A., R. Wanninkhof, T. Takahashi, and P. Tans (1999), The influence of El Niño on the equatorial Pacific contribution to atmospheric CO_2 accumulation, *Nature*, *398*, 597–601.
Feely, R. A., C. L. Sabine, K. Lee, W. Berelson, J. Kleypas, V. J. Fabry, and F. J. Millero (2004a), Impact of anthropogenic CO_2 on the $CaCO_3$ system in the oceans, *Science*, *305*, 362–366.
Feely, R. A., C. L. Sabine, R. H. Byrne, and D. Greeley (2006), Direct evidence for ocean acidification of the North Pacific Ocean *EOS Trans. AGU*, *87*(52), Fall Meeting Supplement, Abstract OS12B-04.
Feely, R. A., C. L. Sabine, J. M. Hernandez-Ayon, D. Ianson, and B. Hales (2008a), Evidence of upwelling corrosive "acidified" water onto the continental shelf, *Science*, *320*, 1490–1492.
Feely R. A., et al. (2008b), *Carbon Dioxide, Hydrographic, and Chemical Data Obtained During the R/Vs Roger Revelle* and *Thomas G. Thompson* Repeat Hydrography Cruises in the Pacific Ocean: CLIVAR CO_2 Sections P16S_2005 (9 January–19 February 2005) and P16N_2006 (13 February–30 March, 2006), edited by A. Kozyr, ORNL/CDIAC-155, NDP-090, Carbon Dioxide Inf. Anal. Cent., Oak Ridge Natl. Lab., US Dep. of Energy, Oak Ridge, Tenn., doi:10.3334/CDIAC/00002.
Feely, R. A., S. C. Doney, and S. R. Cooley (2009a), Ocean acidification: Present conditions and future changes in a high-CO_2 world, *Oceanography*, *22*(4), 36–47.
Feely, R. A., J. Orr, V. J. Fabry, J. A. Kleypas, C. L. Sabine, and C. Langdon (2009b), Present and future changes in seawater chemistry due to ocean acidification, in *Carbon Sequestration and Its Role in the Global Carbon Cycle*, edited by B. J. McPherson and E. T. Sundquist, pp. 175–188, AGU, Washington, D. C., doi:10.1029/2005GM000337.
Feely, R. A., C. L. Sabine, R. H. Byrne, F. J. Millero, A. G. Dickson, R. Wanninkhof, A. Murata, L. A. Miller, and D. Greeley (2012), Decadal changes in the aragonite and calcite saturation state of the Pacific Ocean, *Global Biogeochem. Cycles*, *26* GB3001, doi:10.1029/2011GB004157.
Feely, R., and C. Sabine (2011), *Carbon Dioxide and Hydrographic Measurements During the 2007 NACP West Coast Cruise*, Carbon Dioxide Inf. Anal. Cent., Oak Ridge Natl. Lab., US Dep. of Energy, Oak Ridge, Tenn., doi:10.3334/CDIAC/otg.CLIVAR_NACP_West_Coast_Cruise_2007.
Feely, R., A. Dickson, D. Hansell, C. Carlson (2004b), *Carbon dioxide, Hydrographic, and Chemical Data Obtained During the R/V Melville* Cruise in the Pacific Ocean on CLIVAR Repeat Hydrography Sections P02_2004 (15 June–27 August, 2004), Carbon Dioxide Inf. Anal. Cent., Oak Ridge Natl. Lab., US Dep. of Energy, Oak Ridge, Tenn., doi:10.3334/CDIAC/otg.CLIVAR_P02_2004.
Gattuso, J.-P., and L. Hansson (2011), *Ocean Acidification*, Oxford Univ. Press, Oxford.
Harris, K. E., M. D. DeGrandpre, and B. Hales (2013), Aragonite saturation state dynamics in a coastal upwelling zone, *Geophys. Res. Lett.*, *40*, 2720–2725, doi:10.1002/grl.50460.
Hill, A. E., B. M. Hickey, F. A. Shillington, P. T. Strub, K. H. Brink, E. D. Barton, and A. C. Thomas (1998), Eastern boundary currents: A pan-regional review, in *The Sea*, vol. 11, edited by A. R. Robinson and K. H. Brink, pp. 29–68, John Wiley, New York.
Johnson K. M., et al. (2002), *Carbon Dioxide, Hydrographic and Chemical Data Obtained During the Nine R/V Knorr* Cruises Comprising the Indian Ocean CO_2 Survey (WOCE Sections I8SI9S, I9N, I8NI5E, I3, I5WI4, I7N, I1, I10, and I2; December 1, 1994–January 22, 1996), edited by A. Kozyr, ORNL/CDIAC-138, NDP-080, Carbon Dioxide Inf. Anal. Cent., Oak Ridge Natl. Lab., US Dep. of Energy, Oak Ridge, Tenn., doi: 10.3334/CDIAC/otg.ndp080.
Key, R. M., A. Kozyr, C. L. Sabine, K. Lee, R. Wanninkhof, J. L. Bullister, R. A. Feely, F. J. Millero, C. Mordy, and T.-H. Peng (2004), A global ocean carbon climatology: Results from Global Data Analysis Project (GLODAP), *Global Biogeochem. Cycles*, *18* GB4031, doi:10.1029/2004GB002247.
Key, R. M., et al. (2010), The CARINA data synthesis project: Introduction and overview, *Earth Syst. Sci. Data*, *2*, 105–121, doi:10.5194/essd-2-105-2010.
Kim, T.-W., G.-H. Park, D. Kim, K. Lee, R. A. Feely, and F. J. Millero (2015), Seasonal variations in the aragonite saturation state in the upper open-ocean waters of the North Pacific Ocean, *Geophys. Res. Lett.*, *42*, 4498–4506, doi:10.1002/2015GL063602.
Le Quéré, C., et al. (2014), Global carbon budget 2014, *Earth Syst. Sci. Data Discuss.*, doi:10.5194/essdd-7-521-2014.
Lee, K., T.-W. Kim, R. H. Byrne, F. J. Millero, and Y.-M. Lui (2010), The universal ratio of boron to chlorinity for the North Pacific and North Atlantic Oceans, *Geochim. Cosmochim. Acta*, *74*, 1801–1811.
Levitus, S. (1982), Climatological Atlas of the World Ocean NOAA Professional Paper 13, U.S. Department of Commerce.
Lewis, E., and D. W. R. Wallace (1998), *Program Developed for CO_2 System Calculations* ORNL/CDIAC-105, Carbon Dioxide Inf. Anal. Cent., Oak Ridge Natl. Lab., US Dep. of Energy, Oak Ridge, Tenn.
Li, Y.-H., T. Takahashi, and W. S. Broecker (1969), Degree of saturation of $CaCO_3$ in the oceans, *J. Geophys. Res.*, *74*, 5507–5525, doi:10.1029/JC074i023p05507.
Lueker, T. J., A. G. Dickson, and C. D. Keeling (2000), Ocean pCO_2 calculated from dissolved inorganic carbon, alkalinity, and equations for K1 and K2: Validation based on laboratory measurements of CO_2 in gas and seawater at equilibrium, *Mar. Chem.*, *70*, 105–119.
Matsumoto, K., and R. M. Key (2004), Natural radiocarbon distribution in the deep ocean, in *Global Environmental Change in the Ocean and on Land*, edited by M. Shiyomi et al., pp. 45–58, TERRAPUB, Tokyo.
McPhaden, M. J., et al. (1998), The tropical ocean-global atmosphere observing system: A decade of progress, *J. Geophys. Res.*, *103*, 14,169–14,240, doi:10.1029/97JC02906.
Millero, F. J. (1995), Thermodynamics of the carbon dioxide system in the oceans, *Geochim. Cosmochim. Acta*, *59*, 661–677.
Mucci, A. (1983), The solubility of calcite and aragonite in seawater at various salinities, temperatures, and one atmosphere total pressure, *Am. J. Sci.*, *283*, 781–799.
Orr, J. C., et al. (2005), Anthropogenic ocean acidification over the twenty-first century and its impact on calcifying organisms, *Nature*, *437*, 681–686.
Peltola, E., et al. (2005), *Inorganic and Organic Carbon, Nutrient, and Oxygen Data from the R/V Ronald H. Brown* Repeat Hydrography Cruise in the Atlantic Ocean: CLIVAR CO_2 Section A16N_2003a (4 June–11 August, 2003), edited by A. Kozyr, ORNL/CDIAC-149, NDP-085, Carbon Dioxide Inf. Anal. Cent., Oak Ridge Natl. Lab., US Dep. of Energy, Oak Ridge, Tenn., doi:10.3334/CDIAC/otg.ndp085.
Riley, J. P., and M. Tongudai (1967), The major cation/chlorinity ratios in sea water, *Chem. Geol.*, *2*, 263–269.
Sabine, C. L., R. A. Feely, F. J. Millero, A. G. Dickson, C. Langdon, S. Mecking, and D. Greeley (2008), Decadal changes in Pacific carbon, *J. Geophys. Res.*, *113* C07021, doi:10.1029/2007JC004577.
Schuster, U. and E. Mcdonagh (2007), *C. Darvin 74AB20050501 Cruise Data From the 2005 Cruises*, *CARINA Data Set*, Carbon Dioxide Inf. Anal. Cent., Oak Ridge Natl. Lab., US Dep. of Energy, Oak Ridge, Tenn., doi:10.3334/CDIAC/otg.CARINA_74AB20050501.
Suzuki, T., et al. (2013), *PACIFICA Data Synthesis Project*, ORNL/CDIAC-159, NDP-092 Carbon Dioxide Inf. Anal. Cent., Oak Ridge Natl. Lab., US Dep. of Energy, Oak Ridge, Tenn., doi:10.3334/CDIAC/OTG.PACIFICA_NDP092.

Takahashi, T., S. C. Sutherland, D. W. Chipman, J. G. Goddard, C. Ho, T. Newberger, C. Sweeney, and D. R. Munro (2014), Climatological distributions of pH, pCO_2, total CO_2, alkalinity, and $CaCO_3$ saturation in the global surface ocean, and temporal changes at selected locations, *Mar. Chem.*, *164*, 95–125.

Talley, L. D. (2013), Closure of the global overturning circulation through the Indian, Pacific, and Southern Oceans: Schematics and transports, *Oceanography*, *26*, 80–97.

Taylor, J. R. (1997), *An Introduction to Error Analysis: The Study of Uncertainties in Physical Measurements*, 2nd ed., pp. 327, Univ. Sci. Books, Sausalito, Calif.

Troupin, C., et al. (2012), Generation of analysis and consistent error fields using the Data Interpolating Variational Analysis (DIVA), *Ocean Modell.*, *52–53*, 90–101.

Uchida, H., M. Fukasawa, and A. Murata (2005), *WHP P6, A10, I3/I4 Revisit Data Book Blue Earth Global Expedition 2003 (BEAGLE2003)*, vol. 1, 2, JAMSTEC Publication, Yokosuka, Kanagawa Prefecture, Japan.

Uchida H., A. Murata, and T. Doi (2011), *Carbon Dioxide, Hydrographic, and Chemical Data Obtained During the R/V Mirai* Repeat Hydrography Cruise in the Pacific Ocean: CLIVAR CO_2 Section P21_2009 (10 April–3 July, 2009), Carbon Dioxide Inf. Anal. Cent., Oak Ridge Natl. Lab., US Dep. of Energy, Oak Ridge, Tenn., doi:10.3334/CDIAC/otg.CLIVAR_P21_2009.

van Heuven, S., D. Pierrot, E. Lewis, and D. W. R. Wallace (2009), *Matlab Program Developed for CO_2 System Calculations*, Carbon Dioxide Inf. Anal. Cent., Oak Ridge Natl. Lab., US Dep. of Energy, Oak Ridge, Tenn. [Available at http://cdiac.ornl.gov/oceans/co2rprt.html.]

Wanninkhof, R., et al. (2006), *Carbon Dioxide, Hydrographic, and Chemical Data Obtained During the R/V Ronald H. Brown* Repeat Hydrography Cruise in the Atlantic Ocean: CLIVAR CO2 Section A16S_2005 (11 January–24 February, 2005), edited by A. Kozyr, ORNL/CDIAC-151, NDP-087, Carbon Dioxide Inf. Anal. Cent., Oak Ridge Natl. Lab., US Dep. of Energy, Oak Ridge, Tenn., doi:10.3334/CDIAC/otg.ndp087.

Wanninkhof, R., J.-Z. Zhang, M. Baringer, C. Langdon, W.-J. Cai, J. Salisbury, and R. Byrne (2014), *Carbon Dioxide and Hydrographic Measurements During the R/V Ronald H. Brown* GOMECC-2 Cruise (July 21–August 13, 2012), Carbon Dioxide Inf. Anal. Cent., Oak Ridge Natl. Lab., US Dep. of Energy, Oak Ridge, Tenn., doi:10.3334/CDIAC/OTG.COASTAL_GOMECC2.

Wanninkhof, R., L. Barbero, R. Byrne, W.-J. Cai, H. Z. Zhang, M. Baringer, and C. Langdon (2015), Ocean acidification along the Gulf Coast and East Coast of the USA, *Cont. Shelf Res.*, *98*, 54–71.

Wolf-Gladrow, D. A., U. Riebesell, S. Burkhardt, and J. Bijima (1999), Direct effects of CO_2 concentration on growth and isotopic composition of marine plankton, *Tellus B*, *51*, 461–476.

Zeebe, R. E., and D. Wolf-Gladrow (Eds.) (2001), *CO_2 in Seawater: Equilibrium, Kinetics, Isotopes*, *Oceanogr. Ser.*, vol. 65, pp. 346, Elsevier, Amsterdam.